Biosensors and Bioelectronics 213 (2022) 114440

Contents lists available at ScienceDirect

Biosensors and Bioelectronics

journal homepage: www.elsevier.com/locate/bios

Surface plasmon-enhanced fluorescence and surface-enhanced Raman scattering dual-readout chip constructed with silver nanowires: Label-free clinical detection of direct-bilirubin

Smruti R. Sahoo [a,d], Sandy Huey-Jen Hsu [b], Dev-Aur Chou [c], Gou-Jen Wang [d,e,**], Cheng-Chung Chang [a,e,*]

[a] Intelligent Minimally-Invasive Device Center, National Chung Hsing University, Taichung, 40227, Taiwan
[b] Department of Laboratory Medicine, National Taiwan University Hospital, Taipei, 10002, Taiwan
[c] Department of General Surgery, Changhua Show Chwan Memorial Hospital, Changhua, 50544, Taiwan
[d] Department of Mechanical Engineering, National Chung-Hsing University, Taichung, 40227, Taiwan
[e] Graduate Institute of Biomedical Engineering, National Chung Hsing University, Taichung, 40227, Taiwan

ARTICLE INFO

Keywords:
Direct bilirubin
Plasmon
Hot spot
Raman
Fluorescence
Clinical detection

ABSTRACT

It has been found that the direct/total bilirubin ratio (D/T-BIL) is related to the survival rate of COVID-19 pneumonia. The presence of an excessive amount of bilirubin in human blood also causes liver and neurological damage, leading to death. Therefore, upon considering the adverse impact of the presence of excessive bilirubin in human blood, it has become highly imperative to detect bilirubin in a fast and label-free manner. Herein, we designed and constructed a random-crossed-woodpile nanostructure from silver nanowires to form a 3-dimensional plasmonic hotspot-rich (3D-PHS) nanostructure and successfully used it to detect direct bilirubin (D-BIL) in human blood in a label-free manner. The 3D-PHS nanochip provides rich spatial hot spots that are simultaneously responsive to SERS and SPEF effects and consequently, successfully used to measure and characterize D-BIL with a detection limit of ~10 nM, requiring only 10 μL of human serum for rapid screening, which is the first time D-BIL has been detected in a clinically relevant range. This demonstrates a simple, label-free, pretreatment-free potential biosensing technology that can be used in health care units, and further, in the efficient detection of point-of-care testing with a portable spectrometer.

1. Introduction

Combined with clinical and laboratory data, it was found that the investigation and detection of the direct/total bilirubin ratio (D/T-BIL) can enable one to predict the poor survival of COVID-19 pneumonia. [(Araç and Özel, 2021] COVID-19 virus infects the cell via angiotensin-converting enzyme 2 (ACE2) to critically damage tissues of the lung and other organs, such as the liver. Hence, COVID-19 alters T-BIL, serum aminotransferase, and gamma-glutamyl transferase levels in hepatic tissue [Shah et al., 2021]. Bilirubin is a tetrapyrrole compound that is synthesized by reticuloendothelial cells, especially in the liver and spleen, [Carragher, 2014]; therefore, its concentration in the blood can be used as an important indicator to confirm liver function and identify various liver diseases. That is, monitoring the rapidly rising level of free bilirubin is of great importance to avoid any lethal consequences related to jaundice, hyperbilirubinemia or brain hemorrhage [Hansen et al., 2020; Olds and Oghalai, 2015].

There have been many attempts to detect free bilirubin for clinical diagnostics. The most widely used methods are based on the diazo method [Rahman et al., 2008], bilirubin-oxidase method [Lu et al., 2021], vanadate oxidase method, enzyme-based method [Taurino et al., 2013], electrochemical method [Liu and Zhou, 1994], direct spectroscopy [Rahman et al., 2019; Rao et al., 2015], and high-performance liquid chromatography (HPLC) [Xiao et al., 2020]. Overall, these traditional methods have a wide range of limitations in terms of specificity, sensitivity, cost, sample pretreatment procedures, expensive instrumentation, labor intensity and professional training [Rawal et al., 2020]. Considering the above limitations, it is essential to develop a

* Corresponding author. Intelligent Minimally-Invasive Device Center, National Chung Hsing University, Taichung, 40227, Taiwan.
** Corresponding author. Department of Mechanical Engineering, National Chung-Hsing University, Taichung, 40227, Taiwan.
E-mail addresses: gjwang@dragon.nchu.edu.tw (G.-J. Wang), ccchang555@dragon.nchu.edu.tw (C.-C. Chang).

https://doi.org/10.1016/j.bios.2022.114440
Received 1 May 2022; Received in revised form 27 May 2022; Accepted 29 May 2022
Available online 30 May 2022

stable, sensitive, rapid and direct method for the detection of free bilirubin in human blood. The surface-enhanced Raman spectroscopy (SERS) has been considered for the solution because it can provide unique molecular fingerprints from the probe molecules directly [Shan et al., 2018; Gopal et al., 2016]. SERS technology requires a surface plasmon resonance (SPR)-rich substrate that strongly depends on the noble metal species, size and shape of the nanostructures [Jones et al., 2011]. A variety of SPR-rich nanostructured substrates have been designed to optimize the SERS limit of detection in the detection of analytes. That is, the SERS technique has been widely applied for the rapid detection of DNA, cellular proteins, cancer cells, and various organic molecules with ultrahigh sensitivity [Manikandan et al., 2014; Laing et al., 2016].

Surface plasmon-enhanced fluorescence (SPEF), with respect to SERS, is another type of surface-enhanced spectroscopy technique [Moskovits, 1985]. SPR can offer an optical extinction cross section several orders of magnitude higher than that of common fluorophores when excited, which can increase the sample's absorption and emission cross sections with localized SPR (LSPR) [Rao et al., 2015]. On the other hand, once the fluorophore's emission energy couples with SPR at a suitable distance, it can cause the metal to radiate with enhanced intensity in situ as the fluorophore luminescence, which is also referred to as "metal-enhanced the highest fluorescence enhancement factor [Li et al., 2017]. As a matter of fact, the dominating influence of plasmonics in biosensing applications is obvious from many of its novel applications in current scenario (Ahmadivand et al., 2022), such as micro-scale tetrahertz biosensing chips (Ahmadivand et al., 2020), magnetoplasmonic biosensing (Mejía-Salazar and Oliveira, 2018) and recently, more important issue for detection of SARS-COV-2 antibodies (Liu et al., 2020), SARS-COV-2 spike proteins (Ahmadivand et al., 2021) and clinical diagnosis (Qiu et al., 2021) as well"

Keeping simplicity in mind and with the goal of achieving point of care testing (POCT), we developed a three-dimensional plasmonic hot-spot rich (3D-PHS) nanochip to detect D-BIL in blood using SERS and SPEF spectra (Scheme 1). This 3D-PHS nanochip was constructed based on a random crossed-wire AgNW woodpile structure. The finite integration technique (FIT) was used to simulate and determine the electric field enhancement or plasmonic hotspots present in our as-constructed SERS substrates. Overall, the SERS and SPEF efficiencies of the as-constructed 3D-PHS silver nanostructured biosensors were tested label-free on pure direct bilirubin chemical, direct bilirubin doped in FBS and direct bilirubin in blood (serum) to determine their limit of detection and selectivity without any pretreatment or modification with any external molecules.

2. Experiment

2.1. Materials, 2.2. Apparatus and measurements, 2.3. Synthesis of silver nanowires (AgNW), 2.4. Construction of a crossed-wire woodpile substrate to form 3D-PHS, 2.5. Sample preparation for use with the 3D-PHS chip, 2.6. Finite Integration Technique (FIT) Simulations, 2.7 Clinical serum SERS measurements with a 3D-PHS chip are illustrated in the supporting information (ESI).

Characterization of direct-bilirubin (D-BIL) and silver nanowires (AgNWs)-related Results and Discussion (Fig. S2) are also illustrated in the supporting information (ESI)

3. Results and Discussion

3.1. Construction of 3D-PHS chips from AgNW packing and evaluation of SERS and SPEF

The schematics shown in Scheme 1 and Fig. S1 depicting the fabrication of silver nanowire-constructed 3D random crossed-wire woodpile nanostructures through a very conventional sprinkling method. In this way, multilayer-stacked silver nanowire nanostructures (packing alone in the z direction) can be fabricated, and the layer and density on the substrate are determined based on the spray volumes from the nanowire-containing stock solution to a well (0.5 cm × 0.2 mm). After drying, the SERS and SPEF characteristics for these as-prepared silver nanowire-packing nanostructure chips based on rhodamine 6G (Rh6G) were examined to evaluate the optimized silver nanowire-packing layer and density. Fig. 1a shows the AgNW density-dependent SERS intensity of Rh6G. A constant concentration of Rh6G (1 μM) was drop cast onto

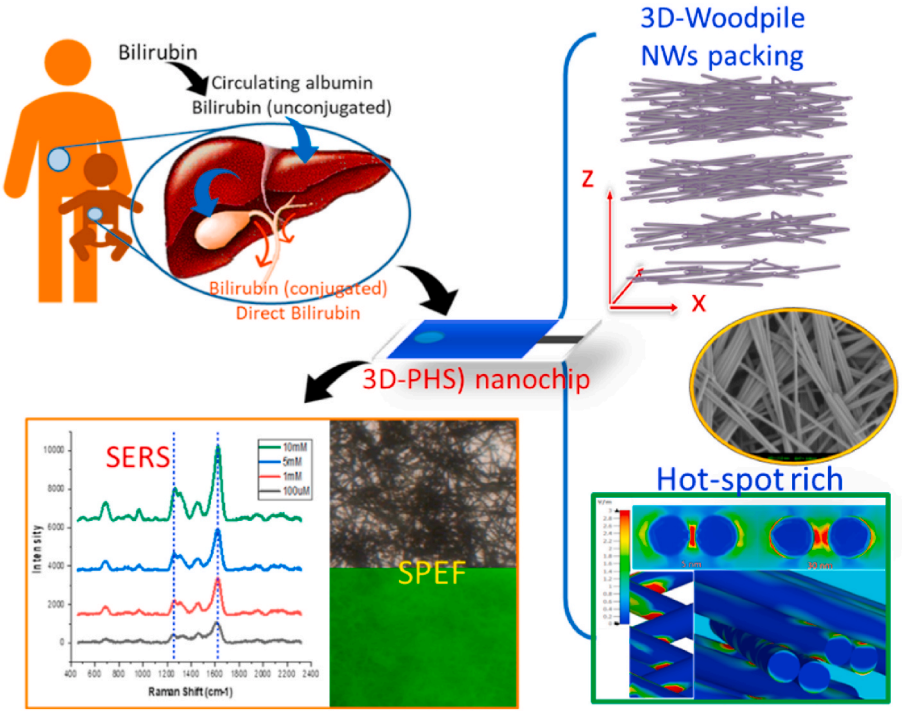

Scheme 1. Construction of three-dimensional plasmonic hot-spot rich (3D-PHS) nanochip and their use in SERS and SPEF detection of analytes.

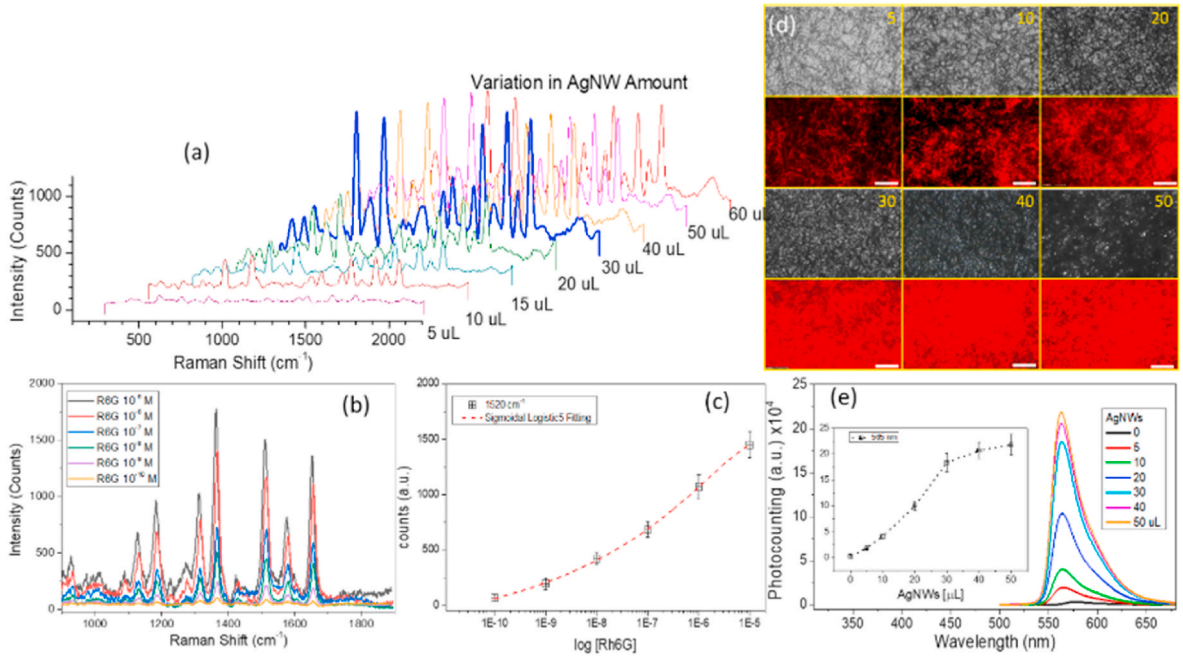

Fig. 1. (a) SERS for Rh6G molecules on the prepared substrate with varying concentrations of AgNWs from 5 to 60 μL. (b) The as-constructed SERS substrates (30 μL from a) can be used to detect Rh6G concentrations as low as 0.1 nM and (c) the fitting curve (sigmoidal Logistic5 fitting with R^2~0.9976). (d) Bright-field (upper) and fluorescent (lower) images. A green-light cube (Ex: 530 ± 20 nm; Em: 590 nm longpass) was used for fluorescence microscopy detection. 10 μL of 10 μM Rh6G was sprinkled onto glass coated with various densities of AgNWs (5, 10, 20, 30, 40, 50 μL). (e) Quantitative fluorescence emission spectra intensities for (a) (Ex: 490 nm). The inset shows a plot of the emission intensities at a wavelength of 565 nm.

the prefabricated variable mounts of crossed-wire woodpile nanostructure substrates. Most of the Rh6G SERS vibrational modes can be assigned to its molecular structure, and all the characteristic Rh6G peaks are observed to be present, as reported in the literature [Xu et al., 2021]. Here, every SERS peak represents an average spectrum from eight different spectra collected at different points, and Fig. S3a presents data for reproducible repeatability with a data error distribution of ~10%. The SERS peak intensities from R6G molecules show an increasing tendency with increasing AgNW amounts (from 5 to 30 mL). A further increase in the AgNW packing density (>30 mL) leads to the observation of a decreasing tendency for the SERS peak intensities.

Furthermore, the stability of the 3D-PHS chip was tested, and the Rh6G SERS signals could still be detected when the prepared chip was placed in the atmosphere for over 80 days (Fig. S3b). On the other hand, the signal intensity decreased for more than 30 μL of Ag NW spreading, which can be explained by the fact that too many layers of nanowires stack with a higher 3D nanostructure density, which will decrease the penetration of both the input light source and output SERS signal. That is, transmittance is the criterion for nanowire packing, which is used to build an optimized 3D-RCW for SERS measurement. Eventually, we chose the optimized 3D-PHS substrate to evaluate the detection limit with varying Rh6G concentrations (Fig. 1b). The Rh6G concentration-dependent SERS intensity at 1510 cm^{-1} is depicted in Fig. 1c. It is evident that the 3D-PHS AgNW SERS substrates can be used to detect Rh6G concentrations as low as 0.1 nM, with an R^2 value of 0.9976. Here, these data were achieved with a very high specification criterion with a CCD integration time of 1 s, and a small volume (10 μL) of solution was used.

The broad absorption shown in Fig. S2a indicates that the plasma energy distribution of the as-prepared AgNW system covers the visible wavelength range, as described in the Introduction, and is suited for SPEF applications of most commercially available fluorophores. We also checked the SPEF effect of the 3D-PHS chip using a standard compound (Rh6G). Fig. 1d shows apparent plasmonic emission-enhancement contrast images for R6G with and without AgNWs obtained by fluorescence microscopy, and the 3D-PHS density-dependent SPEF was evaluated by using a similar investigation method. Fig. 1e shows that the emission enhancement is proportional to the AgNW network density before the emission flattens out, and eventually, in solid-state testing, the SPEF effect of 3D-PHS on Rh6G increases by more than 1000-fold compared to that of free Rh6G.

3.2. *Finite integration technique (FIT) simulations for the 3D-PHS substrates*

Detailed FIT simulation calculations and parameter settings are listed in Experiment section 2.6. Fig. 2a indicates that the incident wave is polarized along the x-direction and that the electromagnetic field enhancement progresses as a waveform along the transverse axis. Then, the crossed AgNW junction generates an irregular electric field enhancement to become a hot spot due to the interference of waves propagating back and forth across the stacking layers (Fig. 2b [Xu et al., 2011]. Additionally, Fig. 2c shows that the simulation result shows that plasma enhancement also occurs at close AgNWs located side by side in parallel, and the insert SEM image also confirms that these parallel AgNWs actually exist, which leads to the generation of hotspots in the xy-plane direction. In summary, hotspots appear not only at the intersection of the stacks (z-direction) but also in the same layer (xy-direction). Hence, directional plasmonic hotspots can also result when AgNWs are piled upon each other based on single placed closely side by side in parallel to create a 3D-PHS environment based on random crossed woodpile structured AgNWs. Fig. 2d shows the calculated electric field values with respect to the variation in the interwire gaps. This can be fitted with a double exponential decay function:

Fig. 2e and **f** clearly show that more apparent fluorescence highlights occur at the intersection and ends of the nanowires, and we observed that the aspect ratio of the nanowire controls the occurrence of hotspots and/or antennas. The larger aspect ratio nanoneedles present more intersections to reveal more hot spots with fewer antenna effects because of difficult conduction, while shorter nanorods present more bright spots

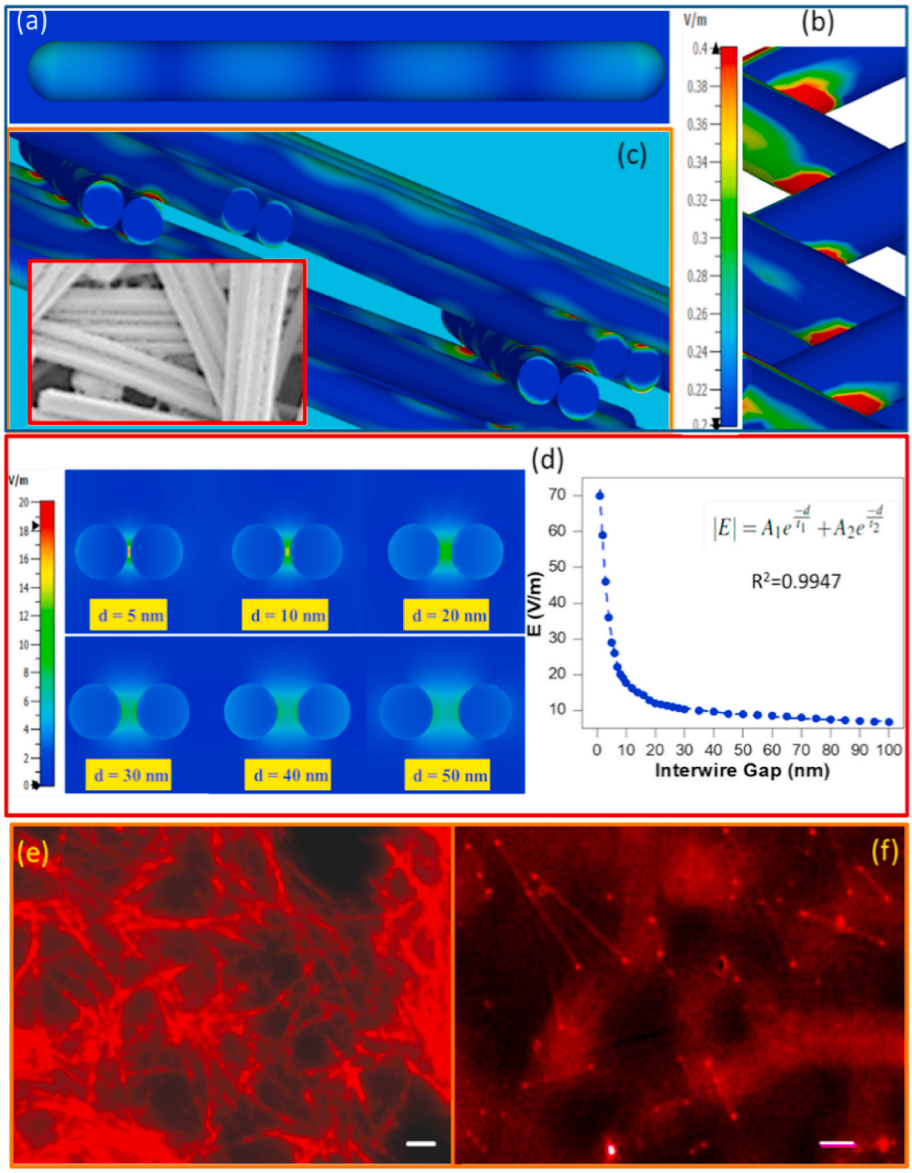

Fig. 2. Finite integration technique (FIT) simulation of AgNWs in 3D-PHS: (a) Electromagnetic field enhancement in a single silver nanowire. (b) A magnified view of the hotspot created at the nanowire junction point. (c) Construction of a AgNW woodpile structure with side-by-side alignment. The insert shows the SEM image in a real 3D-PHS chip. (d) Electric field enhancement related to the distance (gap) between side-by-side nanowires, showing the relation of the generated plasmonic hotspots to the intensity. In all cases, the dimensions of the AgNWs are kept fixed at 1100 nm (length) and 100 nm (width). Measurement and observation of plasmonic hotspots at the intersection or junction points. (e) Hot spot distribution for 3D-PHS at the intersection of nanowires and (f) both ends of the nanorods (b). The green-light cube is used for fluorescence microscopy detection. Scale bar = 5 μm.

at both ends with fewer crossover points (Fig. 2f). That is why we cannot observe a similar result in the nanoparticle system. For 3D nanowire stacking, some reports have determined that cross stacking shows the best simulated electric field enhancement, especially for orthogonal nanowires piled up along the z-direction [Chen et al., 2013; Jeong et al., 2016; Li et al., 2014; Park et al., 2015]. Hence, the maximum electric field enhancement variations of the constructed 3D hotspot region should be stacking-layer dependent. When a 3D AgNW packing system is constructed with a regular hot spot array, the maximum E-field enhancement increases at 5~6 layers of stacking [Jeong et al., 2016]. In our case, as shown in Scheme 1 and Figure S 1, the multilayer AgNW stacks can provide both in-plane (xy-plane) and out-of-plane (z-direction) plasmonic coupling effects. It is reasonable that 30 μL of Ag NW spreading is thick enough to permit measurement of the optical properties and SERS performance as well as the penetration depth limitation for visible light. That is why we observed the synergistic SERS and SPEF effects from the 3D-PHS nanochips.

3.3. Label-free SERS and SPEF detection of bilirubin

The designed 3D-PHS platform in this manuscript not only collects SERS but also enhances the fluorescence from a weak emitter via a 3D plasmon resonance, which can be used to extend the range of a fluorescence biosensor and shows promising potential based on its dual applications in creating large SERS and SPEF enhancements. After successfully confirming the SERS and SPEF dual effects of the 3D-PHS nanochip with Rh6G, we used this platform to evaluate the sensitivity and detection limit toward bilirubin. We checked the solvent effect and found that D-BIL possesses unique absorption peaks and emission peaks located at approximately 450 nm and 515 nm (Fig. S4), respectively. The concentration-dependent SERS spectra for isolated bilirubin (CAS Number 635-65-4) were collected with a laser excitation source operating at wavelength of 532 nm over at least five different points and then averaged. Fig. 3a shows that an increase in the SERS peak intensities can be observed with an increase in bilirubin concentration, and the characteristic SERS peaks for bilirubin match those reported in the literature [Celis et al., 2016; Ouyang et al., 2021]. The strong SERS bilirubin peaks are located at ~677 cm^{-1} (corresponding to the twisting of the C–O bond in the COOH group), ~791 cm^{-1} (in-plane ring deformation), ~970 cm^{-1} (deformation of the methylene bridge), ~1097 cm^{-1} (C–N stretching), ~1245 cm^{-1} (bending of CCH and CCC), and ~1441 cm^{-1} (C–C and C–N mixed stretching and the deformation of C–H and in-plane

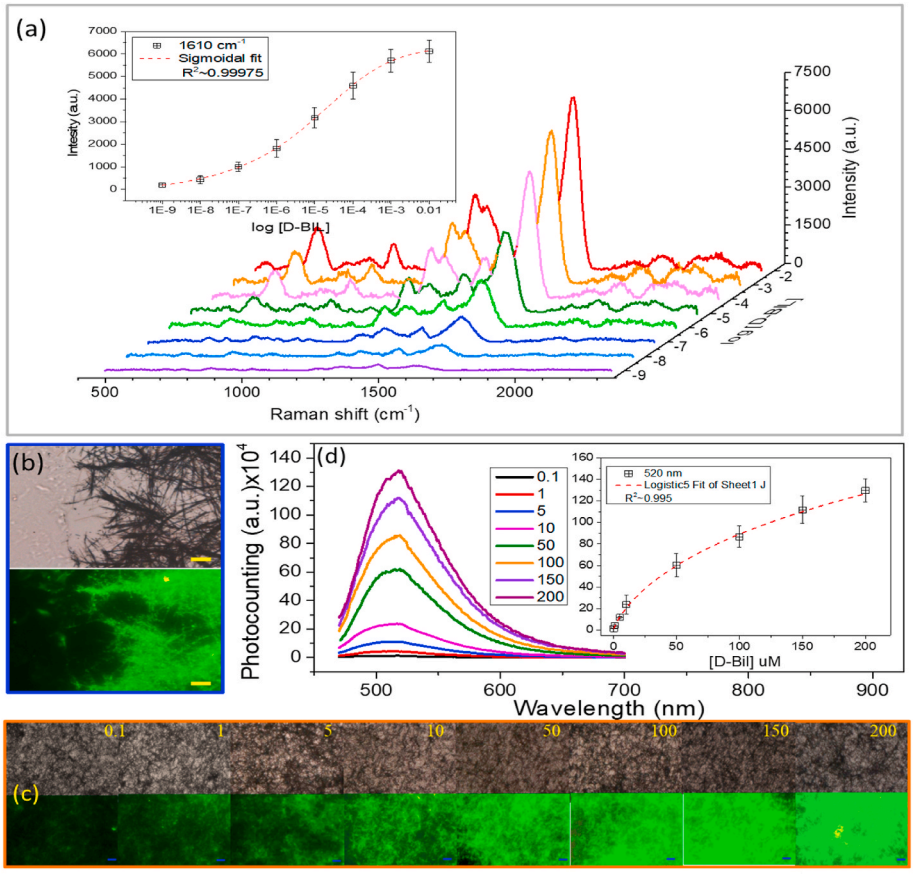

Fig. 3. (a) SERS molecular fingerprints of direct bilirubin chemical at various molar concentrations using a 3D-PHS nanochip. The insert shows that the detection at concentration values down to 1 nM. (b) Bright-field (upper) and fluorescent (lower) images: a proof for SPEF. (c) Varying concentrations of D-BIL (0.1~200 μM) sprinkled onto the surface of the 3D-PHS substrate coated with 30 μL of AgNWs. (d) Fluorescence spectra (Ex: 450 nm) for (b) and their quantitative intensities at 520 nm with sigmoidal growth fitting (R^2~0.995). A blue-light cube was used for this fluorescence microscopy (as described in the Experimental section). Scale bars: 10 μm.

vibration). The most sensitive band in bilirubin is located at ~1610 cm^{-1}, caused by lactam, which is often chosen for quantitative analysis. In particular, bilirubin spectral features are marked by strong correlations at ~677 cm^{-1} and ~1610 cm^{-1}. These features are most likely due to the fact that the ring structures are unperturbed upon bilirubin interaction with silver nanowires. Therefore, we chose the wavelength of 1610 cm^{-1} to evaluate the limit of detection (LOD) for bilirubin by the 3D-PHS nanochip to be as low as the nM level with an R^2 value of 0.9997.

We checked the SPEF effect for D-BIL by using a similar investigation method, and Fig. 3b shows the apparent plasmonic emission-enhancement contrast images obtained for D-BIL with and without AgNWs by fluorescence microscopy. With the help of a color CCD, the green fluorescence of the nanowire matches the D-BIL spectra, which means that the adhesion of D-BIL molecules onto the metal surface and the surface plasma can enhance the weak fluorescence from D-BIL through the SPEF effect. The control assay, as shown in Fig. S5, demonstrates that powder D-BIL reveals a very weak fluorescence intensity, and the AgNWs themselves on the 3D-PHS chip do not emit when excited by a light source, which indicates that D-BIL is a weak fluorescent molecule in the solid-state.

Fig. S6 shows the evaluation of the 3D-PHS density-dependent SPEF, which is found to be in good agreement with the discussion above in that the SPEF effect increases with an increase in the packing amount of AgNWs in 3D-PHS. Hence, the fluorescence intensity of D-BIL reaches the highest value at 40 μL NWs, and then the fluorescence intensity becomes flat and slowly declines. Fig. 3c shows the SPEF detection limit for different D-BIL concentrations on the 3D-PHS. The emission intensity increases with increasing D-BIL concentration, as determined by sigmoidal growth fitting (R^2~0.995). The detection range for D-BIL using the proposed SPEF fluorescence approach was measured, and the detection limit for 3D-PHS is determined to be 0.1 μM (Fig. 3d). Since the normal concentration of D-BIL is below 25 μM, the standard curve obtained can be used for detecting the normal to abnormal threshold for the D-BIL concentration. Nevertheless, SPEF provides an opportunity to detect D-BIL. This is the first time that bilirubin has been detected using fluorescent images and spectra, and this method can complement and be used as a prerequisite test for SERS.

3.4. D-BIL detection in FBS

The SERS molecular fingerprints of bilirubin can be obtained for concentrations as low as 1 nM. The reliability of a SERS substrate is highly essential for biosensing applications, particularly due to its degree of sensitivity and selectivity. Hence, we first added bilirubin to fetal bovine serum (FBS) to prepare FBS solutions containing varying concentrations of bilirubin, and then a 10 μL volume of the as-prepared solution was added directly to the 3D-PHS nanochip, vacuum dried, and subsequently subjected to SERS measurements. Fig. 4a shows the SERS spectra obtained for bilirubin-added FBS samples at different molar concentrations. It can also be observed that all characteristic bilirubin peaks are present in the SERS spectra. In this study, the FBS used as the blood serum shows no detectable bilirubin level. We noted the subtle spectral difference between PBS and serum, resulting from background subtraction rather than the distinct composition (Fig. S7). Apart from modulations at different intensity levels at different wavenumbers, there is no appreciable difference in the SERS spectra obtained in both cases. The 1610 cm^{-1} peak in the bilirubin-spiked FBS system also retains its sharp and intense feature, thereby indicating its potential for use in quantification analysis. A plot of the 1610 cm^{-1} peak intensity against the logarithmic concentration of bilirubin reveals sigmoidal growth fitting with R^2~0.9966 from detection range 10 nM to 0.01 μM (Fig. 4b). The LOD value (10 nM) is calculated to be higher than that shown in Fig. 3, which can be ascribed to the interference from FBS and

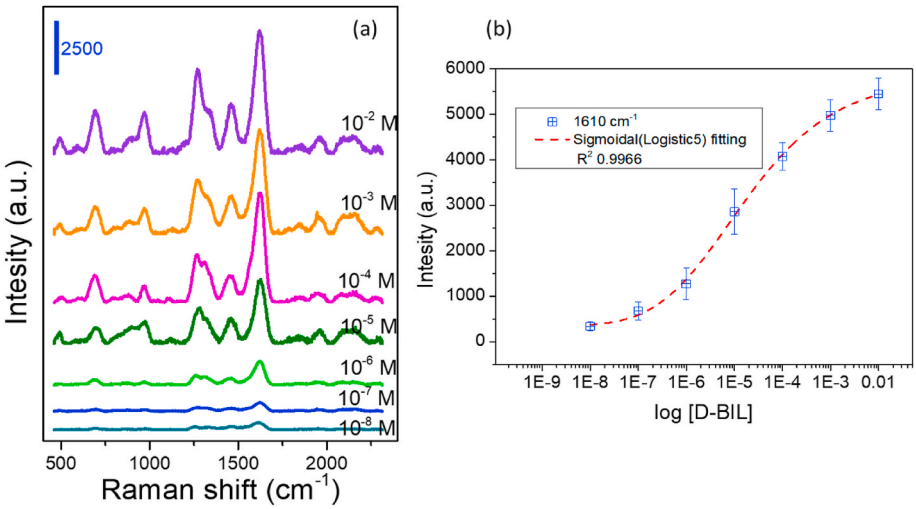

Fig. 4. (a) SERS substrates identify bilirubin molecular fingerprints in bilirubin-containing fetal bovine serum (FBS), indicating good selectivity. (b) Bilirubin in the FBS matrix can be detected down to concentration of 10 nM using the biosensor.

that the system shows more noise at lower bilirubin concentrations.

Serum albumin can bind to free bilirubin with high affinity, forming water-soluble bilirubin complexes [Brodersen and Stern, 1980]; however, these substances existing in blood serum have little effect on the label-free SERS detection of free bilirubin in the present 3D-PHS nanochip. From the result of Fig. S7, the small influence of these biological substances can be accounted for by their low adsorption and small Raman scattering cross-sections on the AgNWs of the substrates. Another control assay was tested to characterize the FBS interference. We first added 70 μl FBS to the 3D-PHS substrates to ensure that FBS covered the whole nanochip. Next, 10 μl of bilirubin with varying concentrations from 5 mM to 10 nM was added directly to the FBS-covered 3D-PHS substrate. Fig. S8 shows that the intensity of the bilirubin SERS spectra gradually increases upon the addition of elevated concentrations of bilirubin. However, a plot of the 1610 cm^{-1} SERS peak against the logarithmic concentration of bilirubin reveals two linear regions ranging from 10 nM to 100 μM and 100 μM to 0.005 M, and a worse LOD is observed. This means that the spread of serum on the metal surface will lead to greater interference for the surface plasma by preventing contact between the nanowire and D-BIL molecule, as shown by SEM in Fig. S8, and this gap will be overcome at higher bilirubin concentrations.

3.5. SERS and SPEF detection of bilirubin in patient serum

To date, there have been no reports of SERS platforms that can be used to detect clinical bilirubin, especially direct bilirubin, in patients. Recently, there have been some reports on the application of SERS to detect bilirubin [Ge, Y. et al., 2022; Geng et al., 2021; Ouyang et al., 2021; Kartashova, A. D. et al., 2021; Vu, T.D. et al., 2020; Pan et al., 2019]. Although this research is mature, the nanochips used for SERS are either too complicated and expensive to manufacture or the D-BIL is not directly measured in the blood. At best, researchers have added bilirubin to serum to simulate the phenomenon of blood testing. In our system, the as-constructed chip was used to detect the presence of bilirubin in human blood to validate the practical exploitation of the present method. As shown in Fig. 4b, we observed that the detection limit in bilirubin-supplemented FBS does not interfere with the SERS signals. With a detection limit of 10 nM, good selectivity toward bilirubin is obtained, and this limit is higher than the level of bilirubin present in human blood. The comparison between 3D-PHS platform and literature reports, as discussed above, was listed in Table S1 (in ESI).

The normal level of free bilirubin in healthy adults is < 25 μM, which in jaundice conditions increases to >50 μM [Geng et al., 2021; Pan et al., 2019; Zou et al., 2018]. This concentration is excessively higher in newborns with hyperbilirubinemia (~ 500 μM) [Bell et al., 2019]. To test the achievement and accuracy of the 3D-PHS for D-BIL detection in human blood, blood serum from twelve volunteers was collected for SERS and SPEF analysis. Fig. 5a shows that these SERS spectra are not apparently different from the experiments above, and the 1610 cm^{-1} Raman peak intensity can be used to quantitatively determine the bilirubin concentration present in human blood serum. Furthermore, we also checked the SPEF tests for serum samples, and Fig. 5b shows real-color (green-yellow) photographs for the fluorescence emission imaging and spectra measurements (in Fig. S9) from the 3D-PHS chips taken through an emission filter and the related measured fluorescence emission spectra for the blood serum.

The hospital results were obtained by using the diazo method with a Beckman Coulter device from the hospital, as described in the experimental section description, which fully obtained bilirubin concentrations varying from ~2 to ~360 μM present in blood samples collected from volunteers. Ultimately, the SERS and SPEF test results reported in this manuscript match the hospital data with small deviations. Here, we also compared the normal/abnormal D-BIL distribution zone, as shown by the red region in Fig. 5d, indicating that the 3D-PHS nanochip is very suitable as a platform tool for human D-BIL detection.

A comparison of the SERS spectra obtained for pure bilirubin chemical, bilirubin-spiked FBS and human serum demonstrated similarity with no appearance of any extra or characteristic peaks in different levels of human blood. Several studies report that the open chain tetrapyrrole can be attracted to noble metals, such as platinum, silver, and gold [Buchler et al., 2007]. This tetrapyrrole open chain present in bilirubin is attracted to the silver nanowire surface and results in an enhanced SERS response, and consequently, increased detection selectivity when using the 3D-PHS nanochip. Moreover, the good selective response might result from the geometrical arrangement of the silver nanowires. The total plasma enhancement is the integrated sum of the contributions from the z-direction and xy-plane hot spots, which provides a greater number of hotspots for shielding bilirubin molecules. Although serum can more or less lead to interference, as found for the FBS condition, this problem is far less serious than that for whole blood. Note that we can increase the accumulation time of the Raman CCD to obtain the finer spectra, not to mention that the detection level for the clinic case is not so low. (the minimum level in this study is ~2 μM)

4. Conclusion

Herein, we designed and constructed a random-crossed-woodpile nanostructure from silver nanowires to form a 3-dimensional plas-

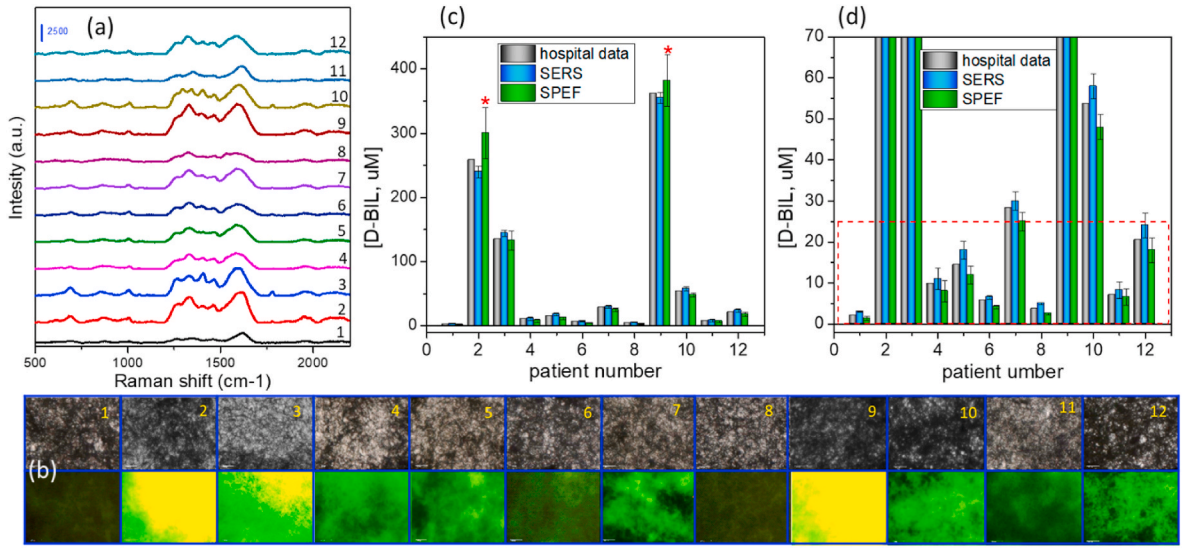

Fig. 5. D-BIL detection for human blood serum (10 μL) using the 3D PHS platform at different clinically relevant concentration levels. (a) Similar molecular fingerprint characteristics with different intensities are observed for D-BIL; (b) SPEF images of the 3D PHS chips in (a) (same optical condition as Fig. 4) and their fluorescence spectra. (c) A histogram representation comparing the results obtained from SERS/SPEF and that from the hospital (black). The red stars represent that concentrations obtained by extrapolation in Fig. 4c. (d) Magnified view of (c) to show the safe D-BIL concentration region (red dashed region).

monic hotspot-rich (3D-PHS) nanostructure and successfully used it to detect direct bilirubin (D-BIL) in human blood in a label-free manner. The 3D-PHS nanochip provides excellent specificity and low interference for complicated biological matrices, without the need for extra sample purification and preparation. Moreover, the 3D PHS nanochip can be synergistically used for SERS and SPEF tests to doubly confirm the test result and D-BIL were successfully measured and characterized with detection limits of ~10 nM requiring only 10 μl of human serum for fast screening, which is the first-time D-BIL has been detected in the clinically relevant range. The 3D PHS nanochip has promising potential as a cheap, robust and portable sensing platform for future applications.

CRediT authorship contribution statement

Smruti R. Sahoo: Writing – original draft, Data curation, Methodology, Software. **Sandy Huey-Jen Hsu:** Data curation, Formal analysis, Writing – original draft, Sample source. **Dev-Aur Chou:** Methodology, IRB. **Gou-Jen Wang:** Investigation, Validation, Writing – review & editing. **Cheng-Chung Chang:** Conceptualization, Supervision, Writing – review & editing.

Declaration of competing interest

The authors declare that they have no known competing financial interests or personal relationships that could have appeared to influence the work reported in this paper.

Acknowledgments

This research was funded by the Ministry of Science and Technology, (MOST 110-2113-M-005-022 -) and (MOST 110-2634-F-005-006 -) of Taiwan.

Appendix A. Supplementary data

Supplementary data to this article can be found online at https://doi.org/10.1016/j.bios.2022.114440.

References

Ahmadivand, A., Gerislioglu, B., Ahuja, R., Kumar Mishra, Y., 2020. Mater. Today 32, 108–130.
Ahmadivand, A., Gerislioglu, B., 2022. Laser Photon. Rev. 16, 2100328.
Araç, S., Özel, M., 2021. Int. J. Clin. Pract. 75 (10), e14557.
Ahmadivand, A., Gerislioglu, B., Ramezani, Z., Kaushik, A., Manickam, P., Ghoreishi, S. A., 2021. Biosens. Bioelectron. 177, 112971.
Bell, J.G., Mousavi, M.P.S., Abd El-Rahman, M.K., Tan, E.K.W., Homer-Vanniasinkam, S., Whitesides, G.M., 2019. Biosens. Bioelectron. 126 (1), 115–121.
Brodersen, R., Stern, L., 1980. Crit. Rev. Clin. Lab Sci. 11, 307–399.
Buchler, J.W., Dreher, C., Künzel, F.M., 2007. Berlin, Heidelberg, 1–69.
Carragher, F., 2014. Churchill Livingstone 484–496.
Celis, F., Campos-Vallette, M.M., Gómez-Jeria, J.S., Clavijo, R.E., Jara, G.P., Garrido, C., 2016. Spectrosc. Lett. 49 (5), 336–342.
Chen, M., Phang, I.Y., Lee, M.R., Yang, J.K.W., Ling, X.Y., 2013. Langmuir 29 (23), 7061–7069.
Ge, Y.C., Wang, F., Yang, Y., Xu, Y., Ye, Y., Cai, Y., Zhang, Q., Cai, S., Jiang, D.F., Liu, X., Liedberg, B., Mao, J., Wang, Y., 2022. Small 18, 2107027.
Geng, Z.Q., Xu, D., Song, Y., Wang, W.P., Li, Y.P., Han, C.Q., Yang, G.H., Qu, L.L., Ajayan, P.M., 2021. Sensor. Actuator. B Chem. 334, 129634.
Gopal, J., Abdelhamid, H.N., Huang, J.-H., Wu, H.-F., 2016. Sensor. Actuator. B Chem. 224, 413–424.
Hansen, T.W., Wong, R.J., Stevenson, D.K., 2020. Physiol. Rev. 100 (3), 1291–1346.
Jeong, J.W., Arnob, M.M.P., Baek, K.M., Lee, S.Y., Shih, W.C., Jung, Y.S., 2016. Adv. Mater. 28 (39), 8695–8704.
Jones, M.R., Osberg, K.D., MacFarlane, R.J., Langille, M.R., Mirkin, C.A., 2011. Chem. Rev. 111 (6), 3736–3827.
Kartashova, A.D., Gonchar, K.A., et al., 2021. ACS Biomater. Sci. Eng. https://doi.org/10.1021/acsbiomaterials.1c00728.
Laing, S., Gracie, K., Faulds, K., 2016. Chem. Soc. Rev. 45, 1901–1918.
Li, J.F., Li, C.Y., Aroca, R.F., 2017. Chem. Soc. Rev. 46, 3962–3979.
Li, X., Lee, H.K., Phang, I.Y., Lee, C.K., Ling, X.Y., 2014. Anal. Chem. 86 (20), 10437–10444.
Liu, Z., Zhou, X., 1994. Anal. Sci. 10 (1), 95–99.
Lu, Z.J., Cheng, Y., Zhang, Y., Wang, X., Xu, P., Yu, H., Li, X., 2021. Sensor. Actuator. B Chem. 329, 129224.
Manikandan, M., Abdelhamid, H.N., Talib, A., Wu, Hui F., 2014. Biosens. Bioelectron. 55, 180–186.
Mejía-Salazar, J.R., Oliveira, O.N., 2018. Chem. Rev. 118 (20), 10617–10625.
Moskovits, M., 1985. Rev. Mod. Phys. 57 (3), 783–826.
Olds, C., Oghalai, J.S., 2015. Semin. Fetal Neonatal Med. 20 (1), 42–46.
Ouyang, L., Yao, L., Tang, R., Yang, X., Zhu, L., 2021. Sensor. Actuator. B Chem. 340, 129941.
Pan, X., Li, L., Lin, H., Tan, J., Wang, H., Liao, M., Chen, C., Shan, B., Chen, Y., Li, M., 2019. Biosens. Bioelectron. 145, 111713.
Park, S.G., Mun, C., Lee, M., Jeon, T.Y., Shim, H.S., Lee, Y.J., Kwon, J.D., Kim, C.S., Kim, D.H., 2015. Adv. Mater. 27 (29), 4290–4295.
Qiu, G., Gai, Z., Saleh, L., Tang, J., Gui, T., Kullak-Ublick, G.A., Wang, J., 2021. ACS Nano 15, 7536–7546.
Rahman, M.A., Lee, K.S., Park, D.S., Won, M.S., Shim, Y.B., 2008. Biosens. Bioelectron. 23 (6), 857–864.

Rahman, M.M., Ahmed, J., Asiri, A.M., 2019. New J. Chem. 43, 19298–19307.
Rao, W., Li, Q., Wang, Y., Li, T., Wu, L., 2015. ACS Nano 9 (3), 2783–2791.
Rawal, R., Kharangarh, P.R., Dawra, S., Tomar, M., Gupta, V., Pundir, C.S., 2020. Process Biochem. 89, 165–174.
Shah, M.D., Sumeh, A.S., Sheraz, M., Kavitha, M.S., Venmathi Maran, B.A., Rodrigues, K. F., 2021. Biomed. Pharmacother. 143, 112158.
Shan, B., Pu, Y., Chen, Y., Liao, M., Li, M., 2018. Coord. Chem. Rev. 371, 11–37.
Taurino, I., Van Hoof, V., De Micheli, G., Carrara, S., 2013. Thin Solid Films 548, 546–550.
Vu, T.D., Jang, E., Lee, J., Choi, D., Chang, J., Chung, H., 2020. Anal. Chem. 92 (12), 8159–8169.
Xiao, W., Zhi, D., Pan, Q., Liang, Y., Zhou, F., Chen, Z., 2020. Anal. Methods 12 (47), 5691–5698.
Xu, D., Duan, L., Jia, W., Yang, G., Gu, Y., 2021. Microchem. J. 161, 3–9.
Xu, J., Kvasnička, P., Idso, M., Jordan, R.W., Gong, H., Homola, J., Yu, Q., 2011. Opt Express 19 (21), 20493–20505.
Zou, Y., Zhang, Y., Xu, Y., Chen, Y., Huang, S., Lyu, Y., Duan, H., Chen, Z., Tan, W., 2018. Anal. Chem. 90 (22), 13687–13694.